Fabrication and photoluminescent characteristics of $La_2O_3:Eu^{3+}$ nanowires

Lixin Yu, Hongwei Song,* Zhongxin Liu, Linmei Yang and Shaozhe Lu

Received 25th August 2005, Accepted 3rd October 2005
First published as an Advance Article on the web 9th November 2005
DOI: 10.1039/b512087j

One-dimensional $La_2O_3:Eu^{3+}$ nanowires (NWs) and sub-micrometer samples (SMs) were fabricated by a hydrothermal method. Their photoluminescent characteristics were studied and compared. The results indicated that the exciton band in NWs blue-shifted in contrast to SMs. In comparison with the charge transfer (CT) band, the relative intensity of the exciton band in NWs was lower than that in SMs, which was attributed to the more energy transfer from the exciton band to surface defects. Frequency-selective-excitation spectra indicated that there existed three symmetry sites of Eu^{3+} ions in NWs and two sites in SMs. The results of the temperature dependence of $^5D_1$–$^7F_2$ lifetimes indicated that the electronic radiative rate of $^5D_1$–$\sum{}^7F_J$ in the two samples had hardly any variation and the nonradiative transition rate of $^5D_1$–$^5D_0$ in NWs increased slightly.

1. Introduction

Since Iijima reported the synthesis of carbon nanotubes in 1991,[1] one-dimensional (1-D) structures, such as tubes, wires and belts with high aspect ratios have become a research focus of nanometer sciences and technology owing to their considerable potential applications in microscopic physics and nanoscale devices.[2] Moreover, in comparison with zero-dimensional (0-D) nanoparticles, the 1-D structure provided an ideal model for investigating the dependence of optical and electronic properties on dimensionality and size effect.[3] In the past decades, many 1-D structures were successfully fabricated and their properties were investigated with the advance in synthesis.[4–13] Rare earth (RE) compounds were extensively used as high-performance luminescence and display devices. It is expected that smaller size phosphors can improve the luminescent quantum efficiency (QE) and display resolution.[14] Thus, the nanocrystals doped with RE have attracted a large amount of interest. In earlier years, the photoluminescent properties of RE ions in 0-D nanoparticles were intensively investigated, including local symmetry, electronic transition processes, surface effects, *etc*.[14–17] Recently, RE doped 1-D structures have attracted considerable attention in this field. Meyssamy and Yada reported for the first time on the preparation of RE phosphate NWs/nanotubes by a hydrothermal method and RE oxides NWs by a template-directed assembly.[18,19] Subsequently, the other 1-D RE compounds were also reported.[20–22] However, until now the luminescent characteristics between 1-D and the corresponding micrometer-sized materials, the so called bulk ones as well as the 0-D nanoparticles have not been compared to a satisfactory degree. In our previous papers, we reported that the local symmetry and electronic transition processes in 0-D and 1-D $LaPO_4:Eu^{3+}$ powders were remarkably different. The radiative transition rate and QE of $^5D_1$–$\sum{}^7F_J$ in NWs increased greatly in comparison with nanoparticles and the corresponding bulk ones.[23,24] This implies that 1-D NWs doped with RE may be ideal nanosized phosphors. Bulk RE oxides, such as Y_2O_3 and La_2O_3 *etc*. are ideal hosts for photoluminescence and are commercial fluorescent powders. To develop 1-D phosphors, some elementary problems should be considered, for example, if the phenomena observed in $LaPO_4:Eu^{3+}$ NWs are universal. Based on the above point, we fabricated $La_2O_3:Eu^{3+}$ NWs and corresponding SMs, and studied their luminescent characteristics.

2. Experimental

Sample preparation

All samples were prepared by a hydrothermal method. In typical synthesis, 1.3928 g of the highly purified La_2O_3 and 0.0190 g Eu_2O_3 (4 N) (Eu : La = 0.01) were firstly dissolved in concentrated HNO_3. Distilled water (120 ml) was added to the above solution. The final pH value was adjusted to 11–12 with diluted NaOH solution (1 M). After stirring well, the milky colloid solution was poured into several closed Teflon-lined autoclaves and subsequently heated at 120 °C (NWs) and 150 °C (SMs) for 24 h. The obtained suspension was centrifuged at 4000 rpm for 15 min and the supernatant was discarded. The resultant precipitation was washed with distilled water and dried at 50 °C in vacuum conditions. The dried $La(OH)_3$ powders were calcined at 500 °C for 2 h to obtain $La_2O_3:Eu^{3+}$ NWs and SMs.

Measurements

The diffraction pattern, morphology and size were obtained by X-ray diffraction (XRD) using a Cu target radiation resource (λ = 1.54078 Å), transmission electron microscopy (TEM)

Key Laboratory of Excited State Physics, Changchun Institute of Optics, Fine Mechanics and Physics, Chinese Academy of Sciences, 16 Eastern Nan-Hu Road, Changchun, 130033, P. R. China. E-mail: hwsong2005@yahoo.com.cn; Fax: 86-431-6176320

utilizing JEM-2010 electron microscope, and field emission microscopy (FEM). The excitation and emission spectra at room temperature were measured with a Hitachi F-4500 fluorescence spectrometer. In the measurements of temperature-dependent fluorescent dynamics, the samples were put into a liquid–helium cycling system, where the temperature varied from 10 to 300 K. A 266 nm light generated from the Fourth-Harmonic-Generator pumped by the pulsed Nd:YAG laser was used as an excitation source. A Rhodamine 6G dye pumped by the same Nd:YAG laser was used as a site-selective excitation source. The Nd:YAG laser was with a line width of 1.0 cm^{-1}, pulse duration of 10 ns and repetition frequency of 10 Hz. The spectra and dynamics were recorded on a Spex-1403 spectrometer, a photomultiplier and a boxcar integrator and processed by a computer.

3. Results and discussion

3.1 Morphology and structure

Fig. 1 shows the XRD patterns of the samples. The structure of both samples belongs to the hexagonal phase, same as the bulk La_2O_3 powders.[25,26] No additional phases are formed. Fig. 2 shows the TEM and FEM images of La_2O_3 samples. It can be seen that the sample prepared at 120 °C yields NWs, with a width of 10–20 nm and length of ~0.5 μm. As the hydrothermal temperature increased, the size of the sample became large and the morphology was inhomogeneous. The sample prepared at 150 °C contains some sub-micrometer particles with a diameter of ~100 nm and some short rods with a diameter of ~100 nm and length of ~200–300 nm. According to the high resolution TEM image, the inside of NWs crystallized well and the fringe became disordered to some extent. The electron diffraction (Fig. 2d) indicated a single crystal nature. In the course of the hydrothermal reaction, $La(OH)_3$:Eu^{3+} NWs formed, whose structure also had hexagonal symmetry. The growth of NWs is determined by two factors. The surface energy determines the preferential surfaces that will grow, and the growth dynamics determine the final structure.[27] Firstly, $La(OH)_3$:Eu^{3+} nanoparticles formed. Then these nanoparticles self-assembled along the [010] axis direction of $La(OH)_3$ to form 1-D NWs.[28] Thus the system possessed the lowest energy and would keep in a steady state. After sintering, $La(OH)_3$ NWs were transformed to La_2O_3 NWs.

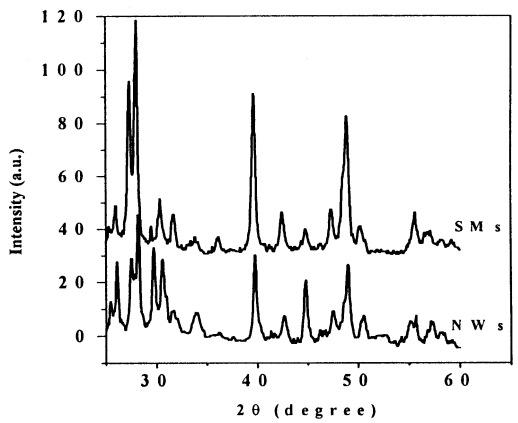

Fig. 1 XRD patterns of La_2O_3:Eu samples.

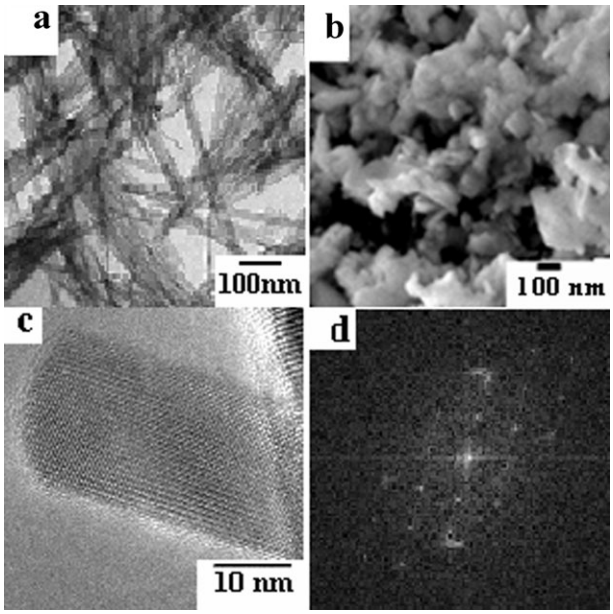

Fig. 2 (a) TEM image of La_2O_3:Eu NWs prepared at 120 °C, (b) FEM image of La_2O_3:Eu SMs prepared at 150 °C, (c) high resolution TEM image of NWs, (d) electron diffraction image of NWs.

In a previous work, we measured the content of Eu^{3+} ions in $LaPO_4$:Eu^{3+} NWs and the corresponding bulk materials prepared by the hydrothermal method.[24] The result indicated that the practical concentration of Eu^{3+} in different samples was nearly the same and approached the doped concentration. For the present work, we suggested that the practical concentration of Eu^{3+} ions in NWs and SMs was the same.

3.2 Luminescent properties

Fig. 3 shows the excitation spectra at 16 367 cm^{-1} at room temperature. In Fig. 3, two intense bands in the range of 50 000–40 000 cm^{-1} and 40 000–33 330 cm^{-1}, respectively, and some weak lines in the range of 28 570–22 220 cm^{-1} were observed, for both samples. The band ranging from 50 000 to 40 000 cm^{-1} is associated with the exciton absorption (EA) of the host, the band of 40 000–33 330 cm^{-1} with the CT transition from the 2p orbital of O^{2-} ions to the 4f orbital of Eu^{3+} ions and the sharp lines between 28 570 and 22 220 cm^{-1} with the direct excitation of f–f shell transitions of Eu^{3+}. Ropp observed that the EA band in La_2O_3 phosphors appeared in all cases, regardless of activators and the exciton energy was 43 480 cm^{-1} (5.4 eV).[26] In Fig. 3, the location of the EA band in NWs was 45 454 cm^{-1} (5.6 eV), while that in SMs was 52 550 cm^{-1} (5.2 eV). The exciton energy in NWs increased compared to that in SMs. For Y_2O_3:Eu^{3+} nanocrystals whose smallest size was about 10 nm and YBO_3:Eu^{3+} nanoparticles whose smallest size was 17.5 nm, the same phenomenon was observed.[29,30] The location of the CT band in NWs (36 900 cm^{-1}) blue-shifted compared to that in SM (35 970 cm^{-1}). Hoefdraad *et al.* reported that the position of the CT band depends on the Eu^{3+}–O distance.[31] The shorter the Eu^{3+}–O distance, the larger the energy difference between

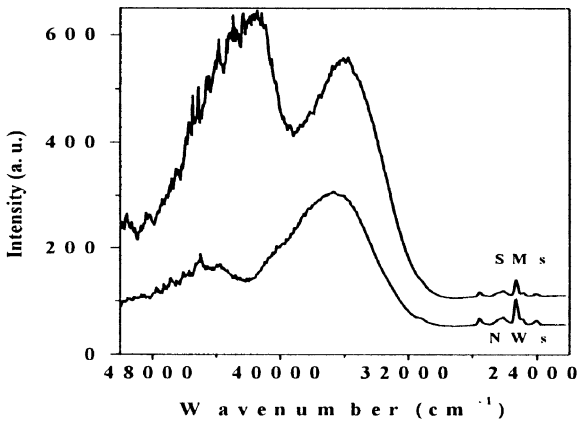

Fig. 3 Excitation spectra monitoring 612 nm at room temperature.

the 4f of Eu^{3+} and 2p electrons of O^{2-} is. Thus, it can be concluded that the Eu^{3+}–O distance in NWs becomes shorter than that in SMs. In Fig. 3, the intensity of the f–f shell transitions had hardly any changes for NWs and SMs. The intensity of EA band in NWs decreased greatly compared to that in SMs, while the intensity of the CT band decreased slightly. In NWs, the surface defects should increase largely compared to those in SMs. We consider that in La_2O_3 NWs, most of the exciton energies were transferred to the surface defects instead of Eu^{3+} ions, causing the intensity of the Eu^{3+} exciton band to decrease. Fig. 4 shows the corresponding emission spectra under 38 460 cm^{-1} excitation. In NWs and SMs, $^5D_{0,1,2}$–^7F_J transition emissions were observed. The detailed origin is labelled in the figure. The integrated intensity ratio of $^5D_{1,2}$–$\sum{}^7F_J$ to $^5D_0$–$\sum{}^7F_J$ was calculated and obtained to be 0.12 in NWs and 0.26 in SMs. It can be seen that the relative intensity ratio of $^5D_{1,2}$–$\sum{}^7F_J$ to $^5D_0$–$\sum{}^7F_J$ increased slightly in SMs in comparison with NWs. We suggested that $^5D_2$–$^5D_1$ and $^5D_1$–$^5D_0$ nonradiative process in NWs become stronger than those in SMs. Thus, $^5D_{1,2}$–$\sum{}^7F_J$ radiative transitions in NWs decreased in comparison with

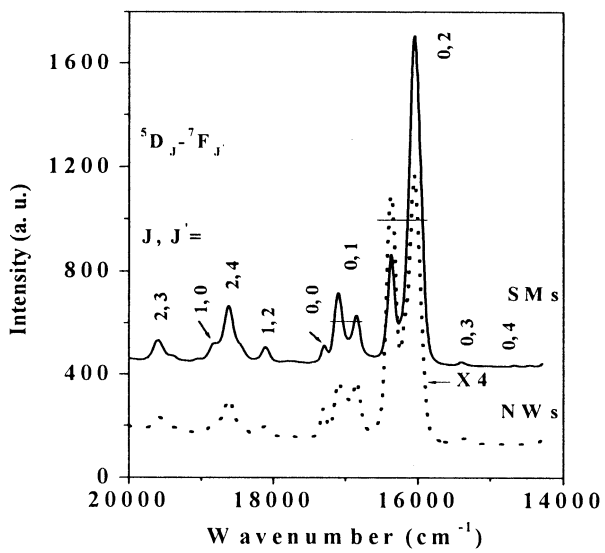

Fig. 4 Emission spectra at 276 nm excitation.

SMs. Due to the larger ratio of surface-to-volume for NWs, large amounts of atoms locate in the fringe. The disorder in the fringe is higher than the inside atoms and produces a great deal of quenching centers for NWs. Therefore, the nonradiative relaxation for $^5D_2$–$^5D_1$ and $^5D_1$–$^5D_0$ in NWs becomes stronger, causing the intensity ratio of $^5D_{1,2}$–^7F_J to $^5D_0$–^7F_J to decrease. The integrated intensity ratio of $^5D_0$–$^7F_2$ to $^5D_0$–$^7F_1$ was obtained to be 3.98 in NWs and 3.97 in SMs, respectively. As is well known, the $^5D_0$–$^7F_1$ lines originate from magnetic dipole transition, while the $^5D_0$–$^7F_2$ lines from the electric dipole one. In terms of the Judd–Ofelt theory,[32,33] magnetic dipole transition is permitted. The electric dipole transition is allowed only on the condition that the europium ion occupies a site without an inversion center and is sensitive to local symmetry. The above results indicated that the relative number of Eu^{3+} at conversion centers hardly changed for both samples. It can also be seen that the relative intensity of the two emission peaks of $^5D_0$–$^7F_2$, located at 16 390 cm^{-1} and 16 050 cm^{-1}, varied greatly in La_2O_3 NWs and SMs. In NWs, the relative intensity of the 16 390 cm^{-1} peak increased largely. This could be attributed to different local environments surrounding Eu^{3+} luminescent centers, which will be discussed in detail in the next section.

3.3 Local symmetry

In La_2O_3, Eu^{3+} ions were substituted for La^{3+} and located at C_3 symmetry site.[19,20] Fig. 5a and b show, respectively, the $^7F_0$–$^5D_0$ excitation spectra monitoring different $^5D_0$–$^7F_2$ sites and the $^5D_0$–$^7F_2$ emission spectra selective exciting $^7F_0$–$^5D_0$ transitions in NWs. In Fig. 5a, as monitoring at 16 334 cm^{-1}, an intense excitation peak at 17 230 cm^{-1} (called A site) appeared, and monitoring at 16 138 cm^{-1} and 16 290 cm^{-1}, a strong peak at 17 210 cm^{-1} (called B site) occurred. As

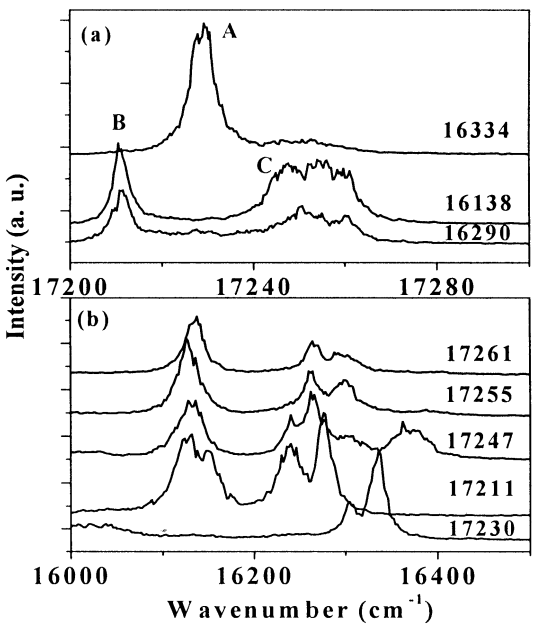

Fig. 5 (a) $^7F_0$–$^5D_0$ excitation spectra monitoring different $^5D_0$–$^7F_2$ sites, and (b) the $^5D_0$–$^7F_2$ emission spectra selectively exciting $^7F_0$–$^5D_0$ transitions in NWs at 77 K. Delay time: 50 μs.

monitoring different $^5D_0$–$^7F_2$ emissions, a broad excitation peak located at 17 255 cm^{-1} (called C site) was observed. The selective-excitation spectra indicated that there existed at least three symmetry sites in NWs. Moune *et al.* systematically investigated the energy levels of Eu^{3+} in La_2O_3 prepared by solid-state reaction.[34] According to their results, there are two excitation peaks of $^7F_0$–$^5D_0$, at 17 231 cm^{-1} and 17 219 cm^{-1}, respectively. At present, the location of sites A and B are 17 230 cm^{-1} and 17 220 cm^{-1}, respectively, which are well consistent with the results of bulk La_2O_3. The C site is an additional one appeared in La_2O_3 NWs. Therefore, we suggest that the site C originated from Eu^{3+} ions in the fringe edge, while the sites A and B from the internal site. According to the high-resolution TEM image, local environments surrounding Eu^{3+} in the fringe edge became disordered in comparison with the internal ones, thus the emission line associated with site C broadened. In Fig. 5b, as excitation corresponds to A, B, and C sites, different group of emission lines are observed. In addition, as exciting different locations of C, 17 247, 17 255 and 17 261 cm^{-1}, the emission spectra changed, indicating that the C site consists of different spectral components. The site-selective excitation experiment demonstrates that the local environments of Eu^{3+} ions at site C are quite different, which is consistent with the results from high-resolution TEM images.

Fig. 6a and b show, respectively, the $^7F_0$–$^5D_0$ excitation spectra monitoring different $^5D_0$–$^7F_2$ sites and the $^5D_0$–$^7F_2$ emission spectra selectively exciting $^7F_0$–$^5D_0$ transitions in SMs. In Fig. 6a, while monitoring at 16 334 cm^{-1}, two intense excitation peaks located at 17 220 cm^{-1} (called B1), 17 231 cm^{-1} (A1) were observed. A1 is fairly sharp and B1 is quite wide. They overlapped to some extent. As monitoring at 16 026 cm^{-1}, a weak peak located at 17 271 cm^{-1} was observed. However, corresponding to the excitation at 17 271 cm^{-1}, no emission line was observed, suggesting that it was probably caused by noise. In Fig. 6b, while exciting A1 and B1 locations, two groups of emission lines appeared. In comparison with the excitation and emission spectra in Fig. 5, it can be seen that site B1 was identical with site B in NWs. Site A1 shifted slightly relative to site A in NWs. Therefore, we suggest that despite the symmetry sites A1 and B1 in La_2O_3 SMs may be as same as those in La_2O_3 NWs as well as the bulk materials.

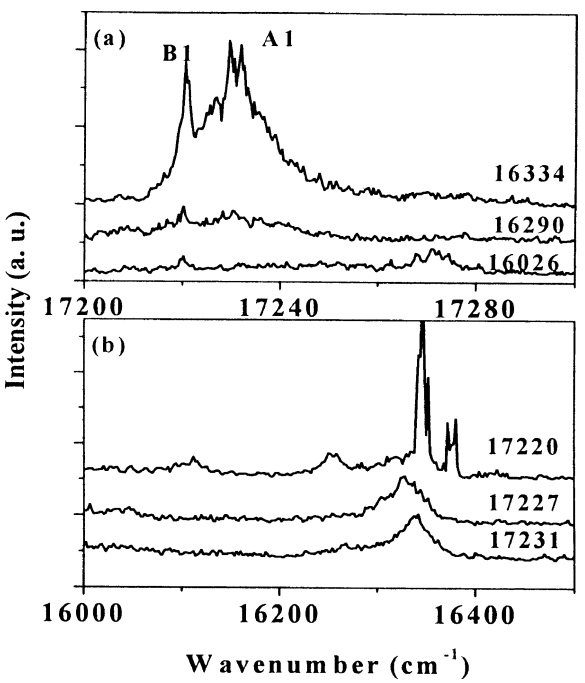

Fig. 6 (a) $^7F_0$–$^5D_0$ excitation spectra monitoring different $^5D_0$–$^7F_2$ sites, and (b) The $^5D_0$–$^7F_2$ emission spectra selective exciting $^7F_0$–$^5D_0$ transitions in SMs at 77. Delay time: 50 μs.

3.4 Electronic transition processes

$^5D_1$ level is a medium excited state among ^5D_J and is suitable for analyzing radiative and nonradiative transition processes. Under a 266 nm excitation, electrons from the ground state were excited to the CT state firstly, and then were fed to excited ^5D_J states. The electrons in $^5D_1$ state came from the nonradiative CT state feeding and $^5D_2$–$^5D_1$ relaxation. Assume that the depopulation processes in $^5D_1$ were contributed mainly to the radiative $^5D_1$–$\sum_J{}^7F_J$ transition, and one-step nonradiative $^5D_1$–$^5D_0$ transition. Then the lifetime of $^5D_1$ can be expressed as[23,24]

$$\tau(T) = \frac{1}{W_1 + W_{10}(T)} \quad (1)$$

where W_1 is the radiative transition rate of $^5D_1$–$\sum_J{}^7F_J$, $W_{10}(T)$ is a nonradiative transition rate at a certain temperature, T. The nonradiative relaxation is a multi-phonon process. According to the theory of multi-phonon relaxation, the lifetime of $^5D_1$ can be expressed as

$$\tau = \frac{1}{W_1 + W_{10}(0)[1 - \exp(-\hbar\omega/kT)]^{-\Delta E_{10}/\hbar\omega}} \quad (2)$$

where $W_{10}(0)$ is the nonradiative transition rate at 0 K, ΔE_{10} is the energy separation between $^5D_1$ and $^5D_0$, $\hbar\omega$ is the phonon energy, k is the Boltzmann' constant. According to eqn (2), if the fluorescence lifetime is measured as a function of temperature, then W_1 and W_{10} can be obtained by fitting.

The fluorescence decay curves of $^5D_1$–$^7F_2$ as well as $^5D_0$–$^7F_2$ were measured at different temperatures. Fig. 7 shows the

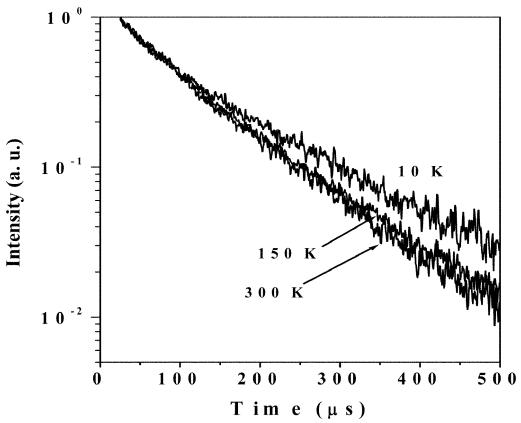

Fig. 7 The decay curves of Eu^{3+} in NWs at 10, 150 and 300 K, respectively, monitoring $^5D_1$–$^7F_2$ emission (18 050 cm^{-1}).

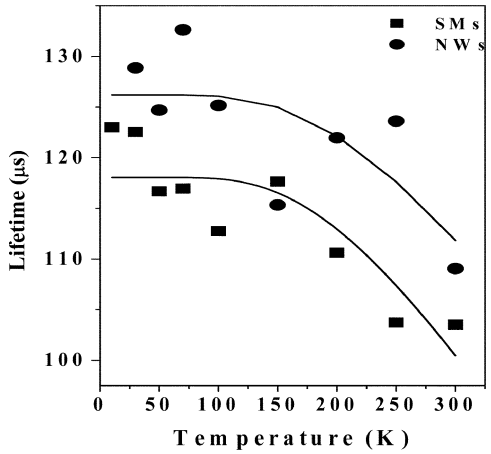

Fig. 8 Dependence of the lifetimes of $^5D_1$–$^7F_2$ transition on the temperature. The scattered dots were experimental data and solid lines were fitting curves.

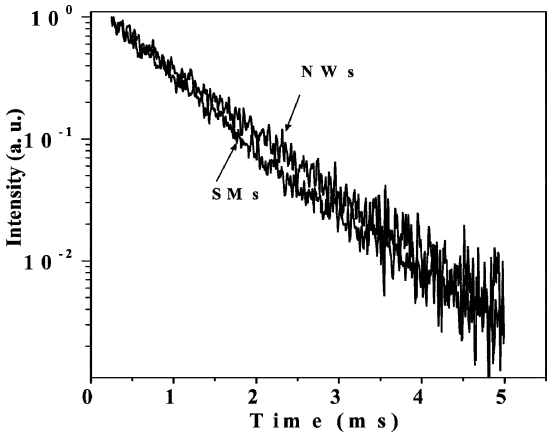

Fig. 9 The decay curves of Eu^{3+} in NWs and SMs monitoring 16 340 cm^{-1} at 10 K.

fluorescent dynamics of $^5D_1$–$^7F_2$ (monitoring: at 18 050 cm^{-1}) for NWs at different temperatures. It can be seen that the $^5D_1$–$^7F_2$ transitions decayed exponentially at any temperature. As the temperature was increased, the fluorescence decay constant became small. Fig. 8 shows the dependence of $^5D_1$–$^7F_2$ exponential lifetimes on temperature. It can be seen that the lifetime of $^5D_1$–$^7F_2$ in the NWs is a little longer than that in SMs, at any temperature. Below $\sim$150 K, the lifetime nearly reserved as a constant. Above 150 K, the lifetime began to slowly decrease with elevated temperature, for both samples. The lifetime from 10 to 300 K had only a little variation. Therefore, it is hard to accurately determine W_1 and $W_{10}(0)$. Despite this, we fitted the experimental data with eqn (2). In the fitting, we chose $\Delta E_{10} = 1758\ cm^{-1}$, $\hbar\omega = 370\ cm^{-1}$. By fitting, W_1 was determined to be $(5.4 \pm 1.2)\ ms^{-1}$ in NWs, and $(4.8 \pm 0.9)\ ms^{-1}$ in SMs. $W_{10}(0)$ was determined as $(3.7 \pm 0.9)\ ms^{-1}$ in NWs, and $(2.6 \pm 1.1)\ ms^{-1}$ in SMs. It seems that the radiative transition rate in NWs increased slightly, while the nonradiative transition rate in NWs increased compared to that in SMs. This was in consistence with the result shown in Fig. 4.

The $^5D_0$–$^7F_2$ fluorescence lifetimes in La_2O_3 NWs and SMs were also measured. Fig. 9 shows the fluorescence dynamics of $^5D_0$–$^7F_2$ in the two different samples monitoring 16 340 cm^{-1}. It can be seen that the $^5D_0$–$^7F_2$ emissions decayed exponentially for both NWs and SMs. The fluorescence decay constant in NWs is slightly longer than that in SMs. The fluorescence lifetimes in NWs and SMs were determined to be 0.82 and 0.73 ms, respectively. The $^5D_0$–$^7F_2$ lifetimes in La_2O_3 hardly changed with the variation of temperature. The $^5D_0$ is the lowest excited state and the energy separation between $^5D_0$ and the nearest downlevel $^7F_6$ is as high as $\sim$12 000 cm^{-1}. In this case, nonradiative relaxation processes hardly happen according to the theory of multi-photon relaxation. Thus we suppose that the radiative transition rate of $^5D_0$–$\sum_J{}^7F_J$ equals the inverse value of the fluorescence decay time. Then, we deduced the radiative transition rate of $^5D_0$–$\sum_J{}^7F_J$, to be 1.22 ms^{-1} in NWs, 1.38 ms^{-1} in SMs. It is obvious that the radiative transition rate of $^5D_0$–$\sum_J{}^7F_J$ in NWs and SMs was nearly the same, too. Unlike in $LaPO_4$:Eu, the radiative transition rate in La_2O_3 has only a slight change between NWs and SMs. In $LaPO_4$:Ce^{3+} and $LaPO_4$:Tb^{3+} NWs and the corresponding micrometer rods, similar results were also observed. However, the electron radiative transition rate and QE remarkably increased in $LaPO_4$:Eu NWs compared to those in the micrometer rods. This means that the radiative transition rate and luminescent QE cannot be improved in any system. The variation of the radiative transition rate in NWs should be dependent on the host materials and the crystal structure, the RE ions and their site symmetry *etc*. This should be investigated further.

Conclusions

La_2O_3:Eu NWs and the corresponding SMs were fabricated by the hydrothermal method and their morphology, size and structure were characterized by XRD patterns and TEM images. The photoluminescent characteristics including local symmetry and electron transition processes were studied and compared. The results indicated that the exciton band in NWs blue-shifted and decreased in comparison with SMs. The relative intensity ratio of $^5D_{1,2}$–$\sum F_J$ to $^5D_0$–$\sum F_J$ in NWs was lower than that in SMs. The site-selective excitation spectra indicated that there existed three symmetry sites in smaller size NWs and two sites in larger size SMs. Moreover, the symmetry sites in both samples changed. The electronic radiative transition rate of $^5D_1$–$\sum{}^7F_J$ and $^5D_0$–$\sum{}^7F_J$ in the two samples hardly changed.

Acknowledgements

The authors gratefully acknowledge financial support by the Nation Natural Science Foundation of China (Grant No. 10504030 and 10374086).

References

1 S. Iijima, *Nature*, 1991, **354**, 56.
2 P. Alivisatos, P. Barbara, A. Castleman, J. Chang, D. Dixon, M. Kline, G. McLendon, J. Miller, M. Ratner, P. Rossky, S. Stupp and M. Thompson, *Adv. Mater.*, 1998, **10**, 1297.

3 Y. Xia, P. Yang, Y. Sun, Y. Wu, B. Mayers, B. Gates, Y. Yin, F. Kim and H. Yan, *Adv. Mater.*, 2003, **15**, 353.
4 S. H. Wang, Q. J. Huang, X. G. Wen, X. Y. Li and S. H. Yang, *Phys. Chem. Chem. Phys.*, 2002, **4**, 3425.
5 X. S. Fang, C. H. Ye, X. S. Peng, Y. H. Wang, Y. C. Wu and L. D. Zhang, *J. Mater. Chem.*, 2003, **13**, 3040.
6 X. S. Fang, C. H. Ye, L. D. Zhang and T. Xie, *Adv. Mater.*, 2005, **17**, 1661.
7 S. Kawasaki, K. Komatsu, F. Okino, H. Touhara and H. Kataura, *Phys. Chem. Chem. Phys.*, 2004, **6**, 1769.
8 X. S. Fang, C. H. Ye, L. D. Zhang, Y. H. Wang and Y. C. Wu, *Adv. Funct. Mater.*, 2005, **15**, 63.
9 C. Rao, F. L. Deepak, G. Gundiah and A. Govindaraj, *Prog. Solid State Chem.*, 2003, **31**, 5.
10 Y. Xia and P. Yang, *Adv. Mater.*, 2003, **15**, 351.
11 Y. Kong, D. Yu, B. Zhang, W. Fang and S. Feng, *Appl. Phys. Lett.*, 2001, **78**, 4.
12 X. Daun, Y. Yang, Y. Cui, J. Wang and C. Lieber, *Nature*, 2001, **409**, 66.
13 Z. Pan, Z. Dai and Z. Wang, *Science*, 2001, **291**, 1947.
14 R. N. Bhargava, D. Gallagher, X. Hong and A. Nurmikko, *Phys. Rev. Lett.*, 1994, **72**, 416.
15 R. S. Meltzer, S. P. Feofilov and B. Tissue, *Phys. Rev. B*, 1999, **60**, R14012.
16 H. Song, B. Chen, H. Peng and J. Zhang, *Appl. Phys. Lett.*, 2002, **81**, 1776.
17 K. Kompe, H. Borchert, J. Storz, A. Lobo, S. Adam, T. Moller and M. Haase, *Angew. Chem., Int. Ed.*, 2003, **42**, 5513.
18 H. Meyssamy and K. Riwotzki, *Adv. Mater.*, 1999, **11**, 840.
19 M. Yada, M. Mihara, S. Mouri and T. Kijima, *Adv. Mater.*, 2002, **14**, 309.
20 M. Yada, T. C. Taniguchi, T. Watari, S. Furuta and H. Katsuki, *Adv. Mater.*, 2004, **16**, 1448.
21 J. Wu, P. Punchaipetch, R. Wallace and J. L. Coffer, *Adv. Mater.*, 2004, **16**, 1444.
22 Y. P. Fang, A. W. Xu, L. P. You, R. Q. Song, J. C. Yu, H. X. Zhang, Q. Li and H. Q. Liu, *Adv. Funct. Mater.*, 2003, **13**, 955.
23 H. Song, L. Yu, S. Lu, T. Wang, Z. Liu and L. Yang, *Appl. Phys. Lett.*, 2004, **85**, 470.
24 L. Yu, H. Song, S. Lu, Z. Liu, L. Yang and X. Kong, *J. Phys. Chem. B*, 2004, **108**, 16697.
25 J. Park, S. Park, C. Kim and H. Park, *J. Mater. Sci. Lett.*, 2001, **20**, 2231.
26 R. Ropp, *J. Electrochem. Soc.*, 1964, **111**, 311.
27 Z. L. Wang, *Adv. Mater.*, 2003, **15**, 432.
28 X. Wang and Y. D. Li, *Chem. Eur. J.*, 2003, **9**, 5627.
29 A. Konrad, T. Fries, A. Gahn, F. Kummer, U. Herr, R. Tidecks and K. Samwer, *J. Appl. Phys.*, 1999, **86**, 3129.
30 Z. Wei, L. Sun, C. Liao, X. Jiang, C. Yan, Y. Tao, X. Hou and X. Ju, *J. Appl. Phys.*, 2003, **93**, 9783.
31 H. Hoefdraad, M. Steglman and G. Blasse, *Chem. Phys. Lett.*, 1975, **32**, 216.
32 B. R. Judd, *Phys. Rev.*, 1962, **127**, 750.
33 G. S. Ofelt, *J. Chem. Phys.*, 1962, **37**, 511.
34 O. Moune, P. Porcher and P. Caro, *J. Solid State Chem.*, 1983, **50**, 41.

